Article

Green Synthesis of Mn + Cu Bimetallic Nanoparticles Using *Vinca rosea* Extract and Their Antioxidant, Antibacterial, and Catalytic Activities

Mohamad M. Ahmad [1],*, Hicham Mahfoz Kotb [1], Shehla Mushtaq [2], Mir Waheed-Ur-Rehman [3], Christopher M. Maghanga [4] and Mir Waqas Alam [1],*

[1] Department of Physics, College of Science, King Faisal University, P.O. Box 400, Al-Ahsa 31982, Saudi Arabia; hkotb@kfu.edu.sa
[2] School of Natural Sciences, National University of Sciences & Technology, Islamabad 44000, Pakistan; shehla.mushtaq@sns.nust.edu.pk
[3] Nanoscience and Nano Technology Unit, Department of Physics, Islamia College of Science and Commerce, Hawal, Srinagar 190001, Jammu and Kashmir, India; mirwaheed250@gmail.com
[4] Department of Biological & Physical Sciences, Kabarak University, Kabarak, Nakuru P.O. Box Private Bag-20157, Kenya; cmaghanga@kabarak.ac.ke
* Correspondence: mmohamad@kfu.edu.sa (M.M.A.); wmir@kfu.edu.sa (M.W.A.)

Abstract: This article outlines the preparation of manganese-doped copper nanoparticles (Mn + Cu NPs) using *Vinca rosea* (L.) leaf extract as a convenient and environmentally friendly substance. UV–vis, FT–IR, XRD, SEM–EDAX, and DLS instrumental techniques were employed to describe the physical and chemical properties of synthesized *V. rosea* extract-mediated *Vr*-Mn + Cu NPs. The synthesized *Vr*-Mn + Cu NPs were observed to be monodispersed and spherical, with an average size of 412 nm. The plant extract includes a variety of phytochemical components. The *Vr*-Mn + Cu NPs also have potential antioxidant and antibacterial properties against selected pathogens. The green synthesized *Vr*-Mn + Cu NPs showed a maximum inhibition zone of 16.33 ± 0.57 mm against *E. coli*. For dye degradation, MR, EBT, and MO showed the highest degradation percentage capabilities with *Vr*-Mn + Cu NP-based adsorbents, which were determined to be 78.54 ± 0.16, 87.67 ± 0.06, and 69.79 ± 0.36. The results clearly show that biosynthesized *Vr*-Mn + Cu NPs may be employed as an antioxidant, antibacterial, photocatalytic dye degradation, and catalytic agent, as well as being ecologically benign.

Keywords: bimetallic; manganese; copper; *Vinca rosea*; antioxidant; antibacterial; dye degradation; catalytic activity

1. Introduction

Nanotechnology plays a vital role in enhanced wastewater treatment and biological therapy as well as in environmental cleanup. Nanoparticles operate as a potential catalyst in the oxidation process to cleanse sewage water from industries due to their chemical, physical, electrical, catalytic, and optical features [1–3]. Due to their excellent properties, nanoparticles are extensively used in medicines, food, optoelectronics, sensors, and cosmetic applications [4–7]. Several biogenic, physical, and chemical methods have been applied to prepare nanoparticles with different morphologies and sizes [8,9].

Bimetallic nanoparticles have recently gained a lot of attention due to their usefulness in a range of disciplines, and their worth comes from their specific features, which are obviously different from those of monometallic nanoparticles [10–13]. When comparing three methods of synthesis, biological synthesis is the least expensive and has more significance than chemical and physical synthesis of nanoparticles, paving the way for a new era, i.e., bio-nanotechnology [14]. Different strategies have been used for the synthesis of nanomaterials, such as the chemical and biological methods. In chemical strategies, different

chemical precursors are used to synthesize the nanoparticle, where most of the chemicals are highly toxic in nature and are considered potential hazards, like for environmental toxicity [15]. The basic use of chemical substances, like organic solvents, reducing agents, and other metallic particles, increases their toxicity. In addition to that, these chemicals limit the colloidal agglomeration and limit the use of nanoparticles in several applications, like clinical and biomedical applications [16]. In addition to the above-mentioned properties, the surface morphology of chemically synthesized nanoparticles is highly dependent on the chemical concentrations and condition of the reaction, such as the different temperatures and pH values. Such nanoparticles have many drawbacks, such as their environmental stability, bioaccumulation/toxicity, expensiveness, and challenges in assembling in devisees. On the other hand, green synthesis is considered as clean, eco–friendly, and biologically appropriate. The green synthesized nanoparticles are considered to have a broad area to study with respect to their shape, size, composition, and physicochemical properties. The biosynthesis approach is a particular stage in producing less costly nanoparticles that are environmentally benign [17,18]. Several environmentally friendly methods of producing various types of bimetallic nanoparticles in solution have been disclosed. Aside from these well-defined/pure reducing agents for the production of nanoparticles, mixture/undefined reducing agents may create noble nanoparticles. Recently, environmental issues, including hazardous wastes and toxic water contaminants, have received a lot of attention. Organic dyes are one of the principal contaminants in wastewater produced by textile and other industrial activities [19–22]. Among the different chemical, physical, and biological strategies for wastewater management, heterogeneous photocatalysis has been identified as a cost-effective choice for water remediation [23]. The superiority of photocatalytic approaches in wastewater treatment is due to its advantages over conventional procedures, such as fast oxidation, the lack of generation of polycyclic products, and the oxidation of pollutants in the ppb range [24,25]. Photocatalysis is a process in which a semiconductor material absorbs light with energy greater than or equal to its bandgap, thereby creating electrons and holes that can then oxidize the substrate in the system. The resultant free radicals are particularly effective oxidizers of organic matter [26,27].

The synthesis of the diverse sizes and forms of semiconductor material nanoparticles has been a popular topic of investigation in recent years. The purpose of these operations is to improve the performance and use of nanoparticles in several applications, ranging from device detection to photonic materials in molecular electronics and enhanced oxidation processes. These nanoparticles' size and shape-dependent electrical and optical characteristics make them an intriguing candidate for use in light-induced chemical reactions. Moreover, biomolecule reductants are thought to be more significant than chemicals. Unquestionably, the concept of biological nanoscience was developed to build unique nanomaterials that are ecologically sustainable and biocompatible with people [28]. These nanoparticles have been shown to have antibacterial, antifungal, insecticidal, and anticancer activities [29,30].

Vinca rosea L is an herbaceous subshrub known as *Lochnera rosea*, *Madagascar periwinkle* around the globe. It is primarily grown for its alkaloids, which have anticancer properties [31]. Vinca's active chemicals fall into two categories: tannins and alkaloids. *Catharanthus roseus* generates hundreds of monoterpenoids and indole alkaloids (TIA) in various organs [32]. The leaves and stems contain dimeric alkaloids, vinblastine, and vincristine, which are essential cancer treatments, while the roots include antihypertensive serpentine and ajmalicine agents [33]. The leaves have long been used to treat diabetes in numerous parts of the globe, including India, Nigeria, and the West Indies [34]. Among other pharmacologically active chemicals, the leaves have been shown to contain 150 valuable alkaloids.

In this present study, green synthesis of bimetallic manganese-doped copper nanoparticles was achieved using *V. rosea* leaf extracts, and their application is discussed in the following sections. The synthesized *Vr*-Mn + Cu NPs were characterized using various techniques including UV–visible analysis, Fourier transform infrared studies, X-ray diffraction analysis, dynamic light scattering, and scanning electron microscopy–energy dispersive

analysis. Most importantly, the applications of the antioxidant, antibacterial, photocatalytic, and catalytic properties for waste management are evaluated.

2. Materials and Methods

2.1. Materials

V. rosea extract was used as both a reducing and capping agent. Copper (II) sulfate ($CuSO_4 \cdot 2H_2O$) and manganese (II) chloride tetrahydrate ($MnCl_2 \cdot 4H_2O$) were used as the precursor materials for the synthesis of the bimetallic nanoparticles. Antioxidant chemicals, Mueller–Hinton broth, Mueller–Hinton agar, and 3-(4,5-dimethylthiazol-2yl) were acquired from Sigma-Aldrich (St. Louis, MO, USA). Methyl red (MR), eriochrome black T (EBT), methyl orange (MO), and 4-nitrophenol were used as pollutants to evaluate the efficiency of the synthesized nanoparticle. All of the purchased chemicals were of a pure and analytical grade. Deionized water was utilized during the entirety of the experiments.

2.2. Plant Collection and Extract Preparation

The plant *V. rosea* was taxonomically identified, and fresh leaves of *V. rosea* were collected from Coimbatore, Tamil Nadu, India (Figure 1). The leaf materials collected from the plants were washed thoroughly using double-distilled water. The leaves were cut into small pieces and ground using a mixer grinder. They were then extracted at a ratio of 1:5 *wt/v* using deionized water, boiled for 45 min after being filtered with Whatman Grade 1 filter paper, and then stored at 4 °C.

Figure 1. *Vinca rosea.*

2.3. Synthesis of Vr-Mn + Cu NPs

The 5 mM $CuSO_4$ and 5 mM $MnCl_2$ were dissolved in double-distilled water (1:1 ratio at 80 mg/mL) and stirred to form a pale blue colloid at room temperature. Then, the aqueous solution of the *V. rosea* plant leaf extract that was prepared was added to the colloid suspension, and stirring continued for 5 min, after which heat was applied at 90 °C. The aqueous solution converted to a dark green color, followed by a clear solution 5 min later. The unreactive plant components and metal precursors were eliminated by centrifuge at 3000 rpm for 10 min and washed using water and ethanol. Then, the *Vr*-Mn + Cu NP solution was air-dried at 28 °C and stored at 4 °C for future use.

2.4. Characterization of Vr-Mn + Cu NPs

The synthesized *Vr*-Mn + Cu NPs were characterized with the help of several analytical techniques, namely UV–vis, FT–IR, XRD, SEM, EDAX, and DLS. UV–visible spectroscopy was evaluated using the Cary UV–visible spectrophotometer, which was carried out using a Shimadzu UV-1800 spectrophotometer (Shimadzu, Kyoto, Japan) within the 200 to 800 nm wavelength. The graph of the bimetallic NPs was plotted with the wavelength on the *x*-axis and the absorbance on the *y*-axis. The FT–IR analysis of the *Vr*-Mn + Cu NPs was completed using the Fourier Transform Infrared Spectrophotometer (Shimadzu 8400S, Kyoto, Japan), which noted the wavelength range from 4000 to 400 cm^{-1}. The composition and morphology of the synthesized bimetallic nanoparticles were found by scanning electron microscopy together with EDAX (SEM, Hitachi S-4700, Tokyo, Japan). The electron dispersive X-ray microanalysis affirms the presence of elemental Mn + Co signals. The particle size analyzer was used to define the size and charge of the synthesized nanoparticles (Horiba SZ 100,Kyoto, Japan). Using the Shimadzu SALD-2300 equipment (WingSALD II: version 3.1.1, Kyoto, Japan), photon correlation spectroscopy (PCS) was employed to measure the mean particle size (Z-average) of the newly synthesized *Vr*-Mn + Cu NPs.

2.5. DPPH Scavenging Activity

The DPPH (2,2-diphenyl-1-picryl-hydrazyl-hydrate) scavenging activity of the bimetallic *Vr*-Mn + Cu NPs was measured using the protocols reported by Gülçin [35], with minor modifications. Different concentrations (200–1000 µg/mL) of the NPs and the standard ascorbic acid were taken in different test tubes. Thereafter, 1 mL of freshly prepared DPPH (0.3 mM) was added to each test tube, vortexed thoroughly, and left to remain at RT for 30 min in the dark to see whether any radical antioxidant reactions occurred. Finally, the optimum density (OD) value of these combinations was determined at 517 nm. The DPPH activity was estimated utilizing the variation in the OD value between the bimetallic NP samples and the control, which refers to the concentrations of the bimetallic NP samples that provide percentages of radical scavenging activity.

2.6. Hydrogen Peroxide Activity

The hydrogen peroxide (H_2O_2) scavenging activity was measured using the bimetallic NPs by adopting the procedure of the study referenced by [36]. For this analysis, H_2O_2 (100 mM) was dissolved in phosphate-buffered saline (PBS) with a pH of 7.4. Then, 300 µL of the solution, containing varying concentrations of *Vr*-Mn + Cu NPs (200–1000 µg/mL), was mixed with 600 µL of H_2O_2 and the final volume was brought up to 1 mL with (100 mM) PBS. The absorbance range was at 230 nm and compared with the individual sample blanks. The percentage of inhibition was then determined using ascorbic acid as the positive control.

2.7. Hydroxyl Radical Scavenging Activity

The extracts were tested for their ability to scavenge hydroxyl radicals using the protocols mentioned by Halliwell and Gutteridge [37]. Briefly, 200–1000 µg/mL of different concentrations of the sample were combined with EDTA solution of 1.0 mL (0.13 g of ferrous ammonium sulphate and 0.26 g of EDTA were dissolved in 100 mL of water). Then, 1.0 mL of DMSO (0.85%) in 0.1 M phosphate buffer (pH 7.4) and 0.5 mL of 0.22% ascorbic acid were added. The reaction was stopped by adding 1.0 mL of ice-cold 17.5% trichloroacetic acid to the reaction mixture, which was maintained in a steam bath at 90 °C for 15 min. All of the test tubes received a Nash reagent of 3.0 mL (3.0 mL glacial acetic acid, 75 g ammonium acetate, and 2.0 mL acetyl acetone in 1.0 L of water) and were kept warm for 15 min for color development. At 412 nm, the absorbance was measured. As a control, the reaction mixture was made without ascorbic acid.

2.8. FRAP

The FRAP (ferric ion reducing antioxidant power) test was performed with slight modifications according to Benzie and Strain's technique [38]. The FRAP chemical was prepared by diluting sodium acetate buffer to 300 mM with a pH of 3.6. Then, 10 mM TPTZ solution was prepared using 40 mM HCl as a solvent and a ferric chloride (20 mM) solution in a volume fraction of 10:1:1 with distilled water. The FRAP reagent was newly made every time and heated to 37 °C by keeping it in a steam bath prior to use. Next, 3 mL of the diluted NP sample was mixed with the FRAP reagent (3 mL). After 4 min, the absorbance of the reaction mix was evaluated at 593 nm. The findings were represented as *Vr*-Mn + Cu NPs, and the ascorbic acid in methanol was employed as a positive control.

2.9. Minimum Inhibitory Concentration (MIC)

The MIC was determined using the methods described by Zhu et al. [39]. For this, 100 mL of Mueller–Hinton broth (MHB) with varying concentrations was used. For the first 10 wells, the NPs were diluted on a flat-bottom 96-well Microtiter plate (Tarsons) and 5 mL of each of the 12 h-old test pathogens was individually introduced to each well. For 12 h, the plates were incubated at 37 °C. Following incubation, 10 mL of the 0.5% freshly prepared MTT (3-(4,5-dimethylthiazol-2-yl)-2,5-diphenlyltetrazolium bromide) was added to all wells and incubated for 2 h in dark conditions, before 100 mL of 2% DMSO (dimethyl sulfoxide) was added as the solubilization solution and incubated for 30 min at room temperature (RT). Following incubation, the OD at 595 nm was measured in an ELISA reader to assess the percentage of cell death. All pathogens were tested against commercially available antibiotic chloramphenicol.

2.10. Antibacterial Activity

The disk diffusion method was used to test the antibacterial efficacy according to Garibo et al. [40]. The bacterial pathogens, such as *Escherichia coli*, *Klebsiella pneumonia*, *Salmonella typhi*, and *Staphylococcus aureus*, were sub-cultured in Mueller–Hinton broth and incubated for 6 h at 35 °C on a shaker at 200 rpm. The sub-cultured strains were then washed with 0.9 percent saline solution until the strain intensity was reached at 0.5 OD at 570 nm. Using sterile cotton swabs, each strain was then swabbed equally on the surface of the individual Mueller–Hinton agar plates and discs were placed inside after adding the required concentration of the NPs. The stock solution of the NPs was prepared as 10 mg/mL concentrations. From the stock solution, 25, 50, and 100 µL was taken to evaluate the antibacterial study. After 24 h of incubation at 37 °C, the zone of inhibition was measured, and the results were mentioned in millimeters (mm). The antibiotic stock solution was prepared by dissolving a 0.1 mg/mL concentration of chloramphenicol, and it was used as a positive control.

2.11. Degradation of Dye using Vr-Mn + Cu NPs

The photocatalytic activity of the *Vr*-Mn + Cu NPs in an aqueous solution against MR, EBT, and MO was investigated. In summary, a stock solution of MR, EBT, and MO (10 mg/L) was prepared using double-distilled water. In a separate flask, 100 mL of MR, EBT, and MO stock solution was added to 10 mg of *Vr*-Mn + Cu NPs. The samples were aliquoted at particular time intervals and centrifuged at 6000 rpm for 5 min before being observed in a UV–vis spectrophotometer for MR (λmax, 522 nm), EBT (λmax, 530 nm), and MO (λmax, 550 nm) to identify the concentration of dye molecules in the solution. The degradation percentage of MR, EBT, and MO was calculated using the following equation:

$$\text{Degradation } (\%) \frac{C_i - C}{C_i} \times 100$$

where C_i denotes the initial concentration of dye solution and C denotes the concentration of dye solution after photocatalytic activity.

2.12. Catalytic Efficiency in Reduction of 4-Nitrophenol

In the 4-nitrophenol reduction, *Vr*-Mn + Cu NPs were used as a catalyst. The reduction reaction was carried out at room temperature. About 1 mM of 4-nitrophenol was dissolved and the solution was made up using deionized water in a standard 100 mL flask. Simultaneously, 50 mg of sodium borohydride was dissolved in 5 mL of deionized water. Sodium borohydride was generally used as a reducing agent. Approximately 20 mL of prepared 4-nitrophenol and sodium borohydride solutions were poured into a 100 mL beaker. Both solutions were allowed to continuously stir for 15 min. Then, 0.25 mg of the *Vr*-Mn + Cu NPs was added to the reaction mixture and stirring was continued for another 5 min. The absorbance values were recorded using a UV–vis spectrophotometer for every 1 min time interval of the reaction mixture. The same procedure was followed for the different catalyst weights, such as 0.5 and 1 mg.

3. Result and Discussion

3.1. UV–Visible Spectrophotometer Analysis

The UV–visible spectrophotometer was used to analyze the formation of the *Vr*-Mn + Cu NPs. Phytochemicals such as alkaloids, terpenoids, triterpenoids, tannins, flavonoids, amino acids, saponins, aromatic acids, and phenolic compounds were found in the *V. rosea* leaf extract and worked as reducing and stabilizing agents [41]. UV–visible spectroscopy was used to examine the solution, and absorbance peaks were noted at 269 and 372 nm, which may be ascribed to the Surface Plasmon Resonance (SPR) effect of the *Vr*-Mn + Cu NPs (Figure 2). The appearance of the SPR band was determined by the shape and size of the NPs as well as the concentration of the reducing agent [42]. A similar finding was discovered in a recent study confirming the creation of green synthesized bimetallic Mn + Cu nanoparticles [43].
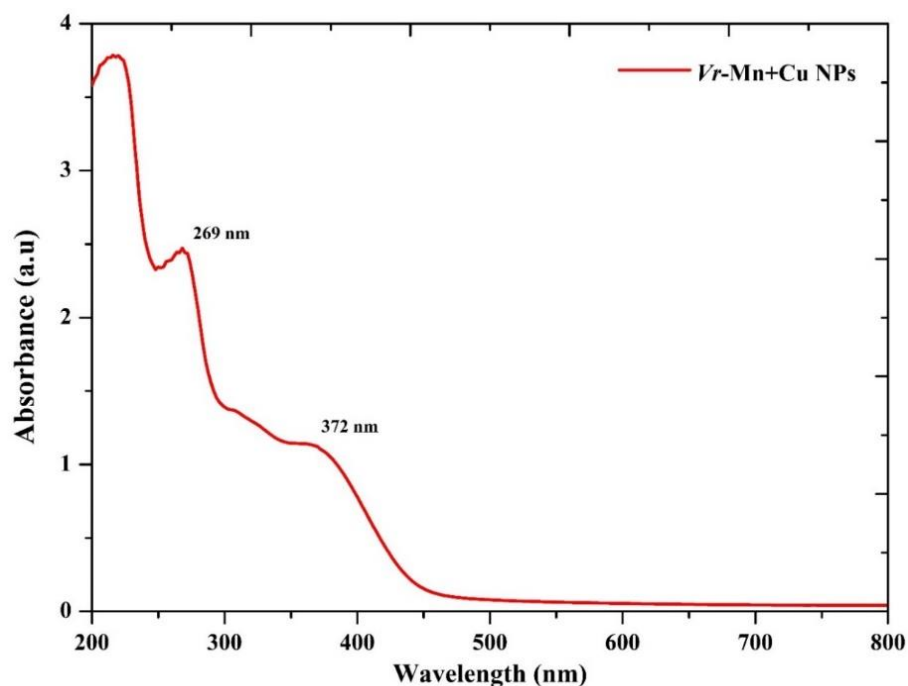

Figure 2. UV–vis analysis of *Vr*-Mn + Cu NPs.

3.2. FT–IR Analysis

The stability and functional groups present in the *V. rosea* and *Vr*-Mn + Cu NPs were identified by FT–IR analysis. During the analysis of *V. rosea*, the broad and small band observations at 3425 and 1648 cm^{-1}, respectively, were due to the stretching and bending vibrations of the water molecules (O–H group) present in the plant extract. The band

detected at 614 cm^{-1} was attributed to the =C–H bending vibration, and the characteristic peak that appeared at 2859 and 2925 cm^{-1} was assigned to the –C–H stretching vibration. The presence of a C–C stretching vibration in the aromatic ring was confirmed by the peak that appeared at 1438 cm^{-1}. The C–N stretching vibration in the aromatic amine and the C–N stretching vibration in the aliphatic amine were verified by the peaks detected at 1257 and 1058 cm^{-1}, respectively. The FT–IR analysis was performed for the *Vr* and *Vr*-Mn + Cu NPs, and it is shown in Figure 3. The broad band was detected at 3415 cm^{-1}, which may be due to the stretching vibration, as the material absorbed the moisture present in the environment. The peak observed at 1627 cm^{-1} was assigned to the bending vibrations of the –O–H group present in the water molecule. The –C–H stretching vibration present in the material was confirmed by the peak, which appeared at 2925 cm^{-1}. The C–O deformation was confirmed by the peak that appeared at 1110 cm^{-1}. The presence of a C=N stretching vibration was verified by the peak at 1389 cm^{-1}. The –C–H stretching vibration was confirmed by the peak observed at 614 cm^{-1}.
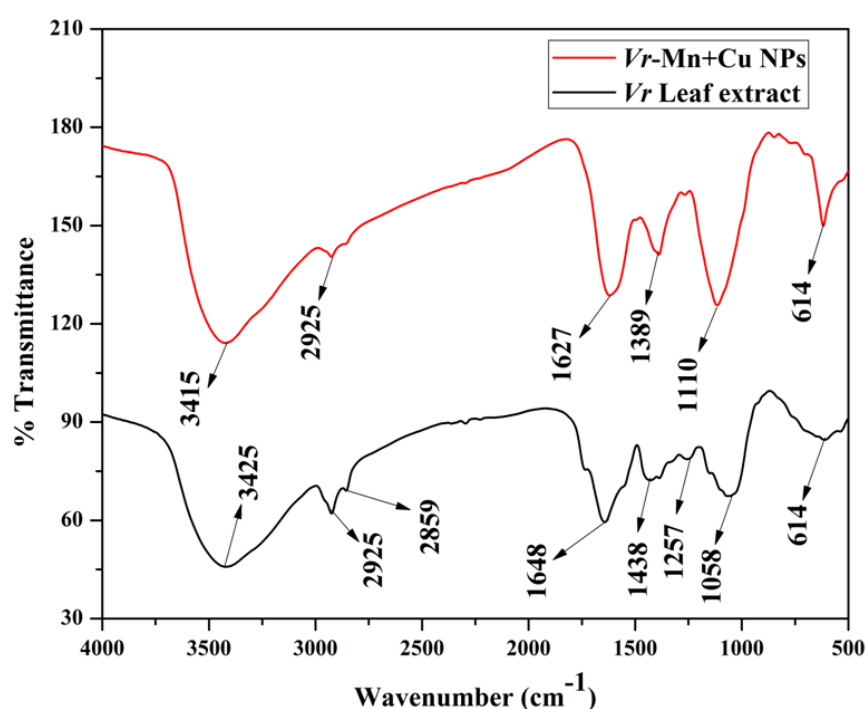

Figure 3. FT–IR analysis of *Vr*-Mn + Cu NPs.

3.3. XRD Analysis

The X-ray diffraction pattern of the *Vr*-Mn + Cu NP is shown in Figure 4. An XRD study is the most important instrument for the qualitative verification of the expected material formation in materials research. The analysis shows characteristic peaks with less intensities and substantial broadening. The inferior intensities are a credit to the hindering effect of amorphous particles. This essentially indicates the formation of nanostructured bimetallic nanoparticles. However, it can appear that noises are observed with incredibly low intensities in the 2θ range between 10° and 90°. This specifies that several amorphous contaminations/phases of the preferred material exist in the synthesized particle, which might be due to the unreactive materials present in the bimetallic particle. The 2θ = 31.84°, 33.35°, 36.20°, 50.83°, 64.42° and 83.64°, which correspond to the Miller indices (002), (200), (111), (112), (020), and (205). The observed XRD pattern of the synthesized bimetallic nanoparticles matches with the JCPDS card no. 65-2308, and the nanoparticle is monoclinic in structure. The crystallite size of the nanoparticle was found to be 19.41 nm. Hemalatha et al. reported the monoclinic crystalline copper-doped manganese

oxide nanoparticles in different ratios ($Cu_{0.975}Mn_{0.025}O$, $Cu_{0.95}Mn_{0.05}O$, and $Cu_{0.9}Mn_{0.1}O$), which had crystallite sizes of 18.7 nm, 20.2 nm, and 22.5 nm, respectively [44].
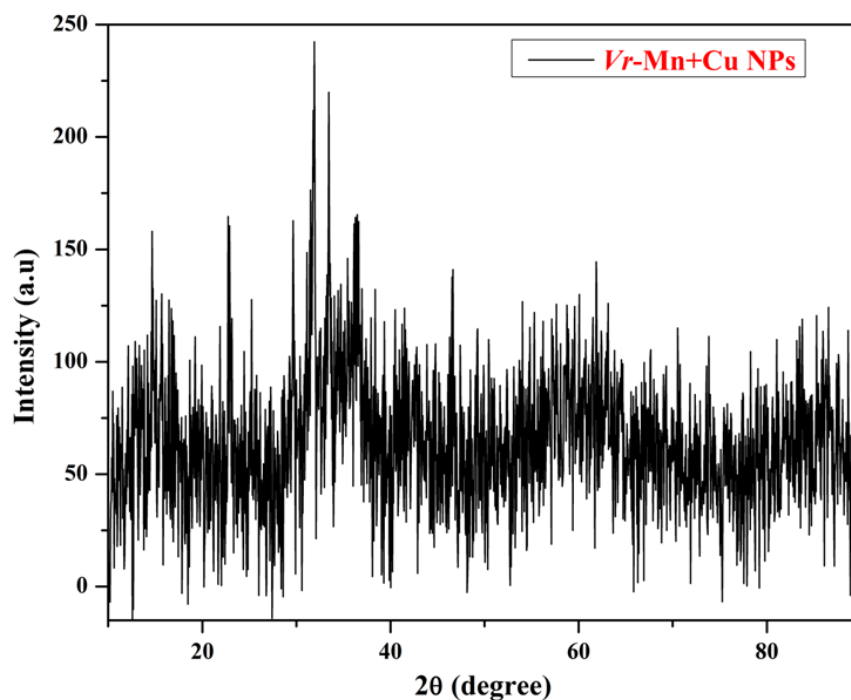

Figure 4. XRD pattern of *Vr*-Mn + Cu NPs.

3.4. SEM and EDX Analysis

A SEM analysis was performed to characterize the green synthesized Mn + Cu NPs. In the micrograph, the particles of the *Vr*-Mn + Cu NPs were spherical in form (Figure 5). The Co NPs were photographed at 10 m magnification, 10.00 kV, WD-9 mm, and Mag-1.00 KX, revealing the morphology of the nanoparticles. The morphology suggests uniform particles, with a confined size variation in the range of the average scale length, which were roughly 420 nm. As synthesized nanoparticles have an exceptionally smooth surface, which allows for increased contact with the bacterial cell wall and thereby enhances the NPs' bacterial growth-inhibiting properties. This kind of behavior of smooth-surfaced nanoparticles has already been shown in the literature [45]. An EDAX analysis indicated the element contained in the particle, atomic, and weight percentage for the *Vr*-Mn + Cu NPs. Figure 5 illustrates the EDX pattern of the *Vr*-Mn + Cu NPs, which demonstrated that a 13.74% copper, 10.36% manganese, and 47.41% oxygen weight was present in the nanoparticles. This substantiates the production of *Vr*-Mn + Cu NPs. This analysis revealed that there were no contaminants in the nanoparticles, by inference of the copper and oxygen peaks alone [46].

3.5. DLS Analysis

A DLS was used to determine the size distribution of the *Vr*-Mn + Cu NPs in a solution under varied synthesis conditions (Figure 6). As the extract concentration Mn and Cu dissolution rises, the nanoparticles become larger and less stable due to their proclivity to agglomerate. *Vr*-Mn + Cu NPs have a very narrow size distribution, with an average dimension size of around 136.9 nm. The negative result validates the repulsion of the particles and establishes their separation. The solvent, pH, and ionic strength all have major impacts on the surface charge of the NP [47]. As a consequence, since Milli-Q water is amphipathic and has no influence on surface charge during analysis, we used it as a solvent. The negative surface charge demonstrated that the NPs were very stable and maintained significant repulsion amongst themselves, thereby preventing nanoparticle aggregation. The charge on the nanoparticles is directly related to their stability [48]. The size and

properties of metallic nanoparticles vary depending on the fabrication technique and the extract-to-salt ratio [49].
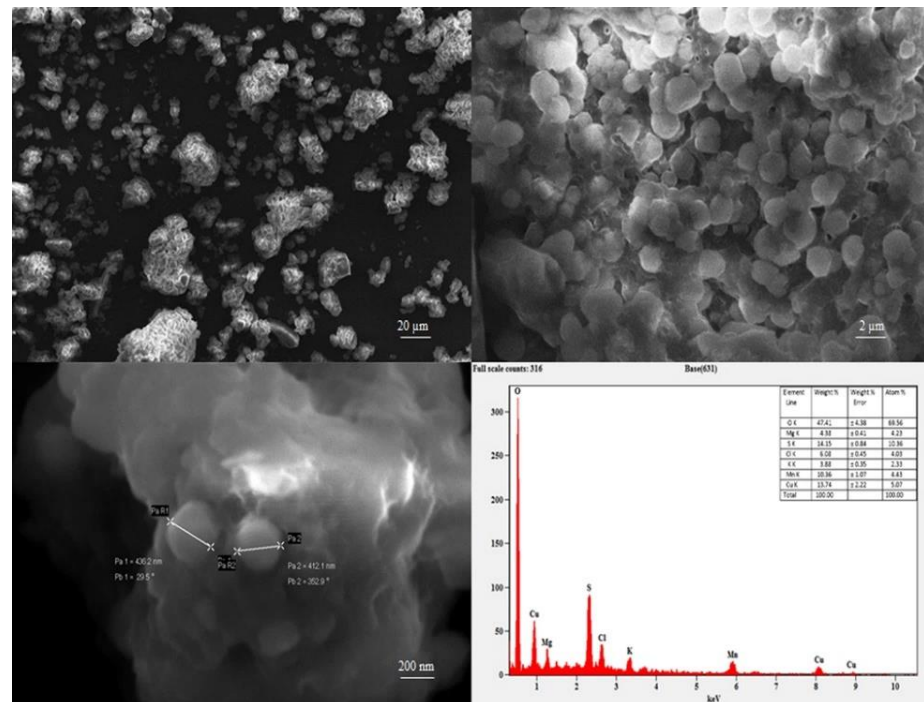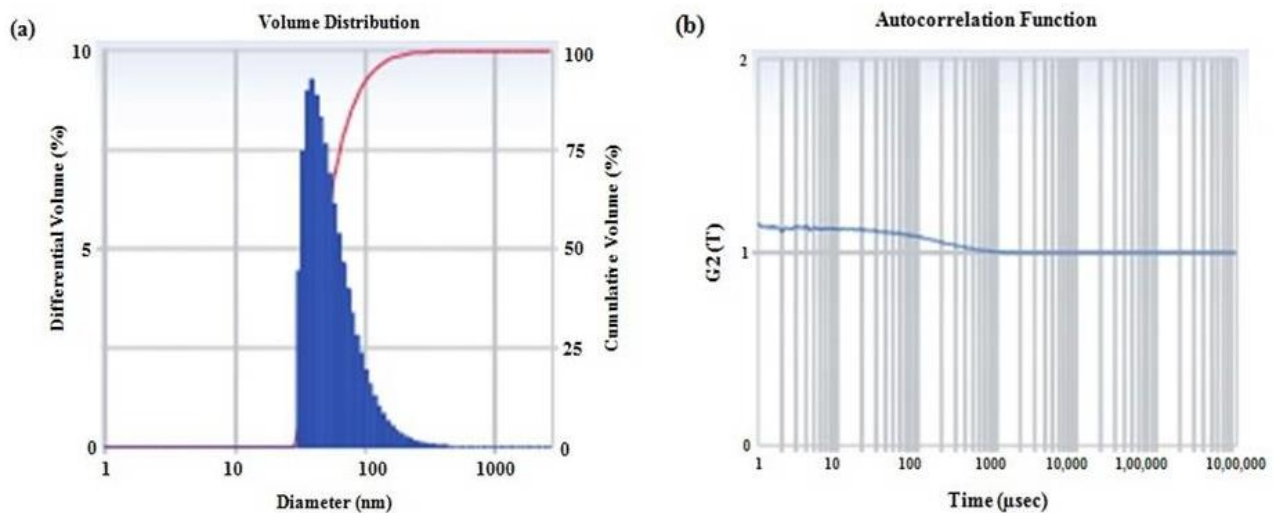

Figure 5. SEM–EDX analysis of *Vr*-Mn + Cu NPs.

Figure 6. DLS analysis of *Vr*-Mn + Cu NPs. (**a**) Volume distribution and (**b**) Autocorrelation function.

4. Antioxidant Activity

4.1. DPPH

A DPPH analysis is a stable free radical well known for its part in decreasing the receipt of hydrogens or electrons from donors [50]. The *Vr*-Mn + Cu NPs' color shift was utilized to assess their DPPH reducing activity. When compared with ascorbic acid, DPPH scavenging activity greatly limited the action of the *Vr*-Mn + Cu NPs (Figure 7a). The *Vr*-Mn + Cu NPs had a high DPPH activity that was dose-dependent. As a consequence, the *Vr*-Mn + Cu NPs displayed more inhibition, with a DPPH scavenging activity of 51.44% for 1000 µg/mL. The antioxidant activity tends to rise with an increase in the concentration of the nanoparticle. The color change was seen after adding the NPs to a DPPH solution,

which, as a consequence of the DPPH scavenging, was mediated by the donation of a hydrogen atom to stabilize the DPPH molecule [51]. The antioxidant activity of the *Vr*-Mn + Cu NPs may be attributed to the functional groups obtained from the maize stem extract.
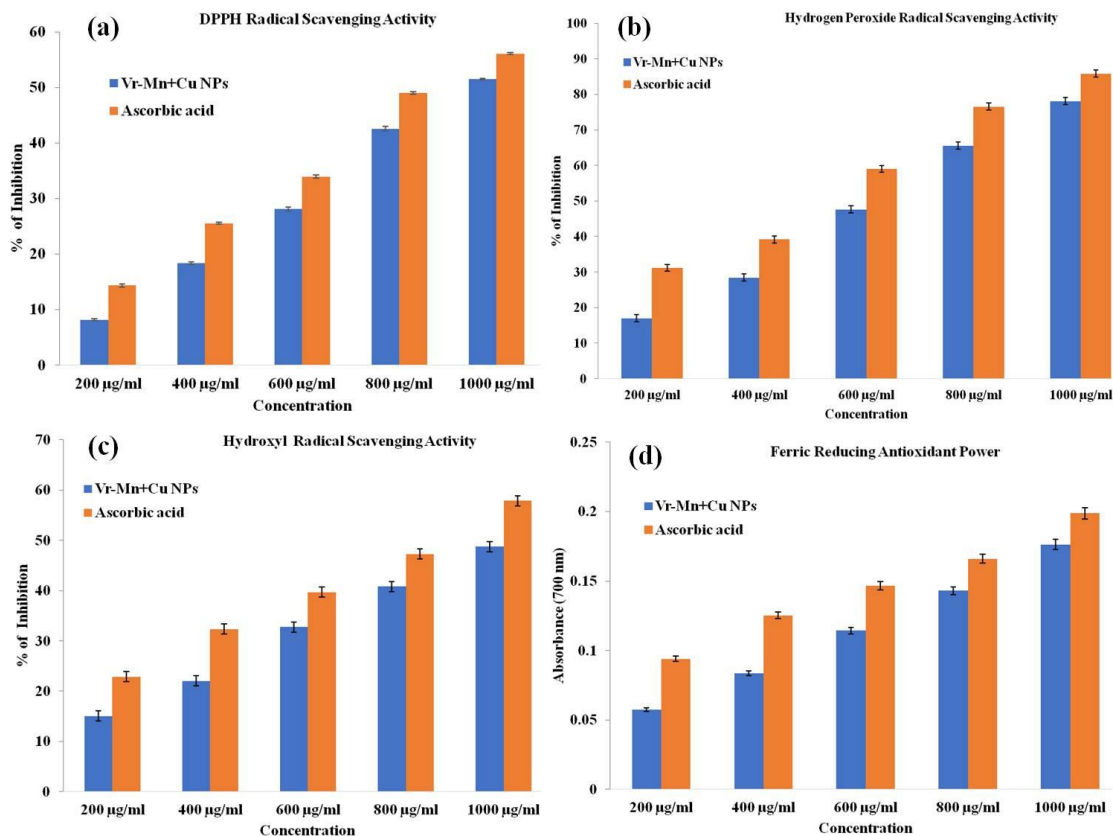

Figure 7. Antioxidant study by *Vr*-Mn + Cu NPs with different assays: (**a**) DPPH; (**b**) H_2O_2; (**c**) hydroxyl radical; and (**d**) FRAP.

4.2. H_2O_2

The hydrogen peroxide (H_2O_2) test is a spectrophotometric method used to detect hydroxyl radicals in biological materials. OH percent radicals, one of the most reactive oxygen species, may promote cell membrane disintegration and membrane protein degradation [52]. OH radical scavengers may be preferable solutions for avoiding tissue damage. In the present work, the percentage of scavenging ability was greater than before with the growing concentration of *Vr*-Mn + Cu NPs (Figure 7b). For the H_2O_2 test, the occurrence of phenolic compounds in the samples is critical. Yang et al. observed a dose-dependent manner of H_2O_2 scavenging activity for Co–Fe NPs and achieved comparable findings [53]. Uninhibited H_2O_2 buildup produces oxygen free radicals (peroxide and hydroxyl), which cause severe destruction to cell membranes in living systems. Spectrophotometry was used to assess the hydrogen peroxide scavenging activity of the *Vr*-Mn + Cu NPs. The inhibitory concentrations of the *Vr*-Mn + Cu NPs and ascorbic acid at 1 mg/mL were found to be 78.08% and 85.35%, respectively.

4.3. Hydroxyl Radical Scavenging Activity

The hydroxyl radical (OH) plays a vital role in the development of carcinogenesis, mutagenesis, and cytotoxicity by causing DNA damage [54]. The *Vr*-Mn + Cu NPs scavenged the OH radical in a dose-dependent manner, as shown in Figure 7c. Biosynthesized *Vr*-Mn + Cu NPs at doses of 0.2, 0.4, 0.6, 0.8, and 1.0 mg/mL inhibited the enzyme by 15.04, 22.02, 32.73, 40.73, and 57.88%, respectively. The standard ascorbic acid showed inhibition at 22.86, 32.37, 39.71, 47.29, and 57.88%, respectively. As OH radicals are involved in the

peroxidation process, the ability of the *Vr*-Mn + Cu NPs to scavenge or suppress OH radicals show that *Vr*-Mn + Cu NPs may considerably reduce lipid peroxidation. The ability of a chemical to reduce this may be an essential indicator of its potential antioxidant action. In contrast to the ascorbic acid, the *Vr*-Mn + Cu NPs have reductive powers. It is also worth noting that the *Vr*-Mn + Cu NPs consistently exhibit a stronger reduction power than DPPH scavenging activity.

4.4. FRAP Assay

The maximum absorbance in the FRAP experiment was 0.198 for standard ascorbic acid and 0.176 for the produced *Vr*-Mn + Cu NPs at 1 mg/mL. At concentrations of 0.2, 0.4, 0.6, and 0.8 mg/mL, the FRAP absorbance values for *Vr*-Mn + Cu NPs were observed as 0.057, 0.083, 0.114, and 0.143, respectively, and the absorbance values for ascorbic acid were 0.094, 0.125, 0.146, and 0.166, respectively. Figure 7d depicts the outcomes of this study. It has been shown that there is a straight link between antioxidant and reducing capacity [38]. The ferric iron (Fe^{3+}) to ferrous iron (Fe^{2+}) conversion assay was used to assess the antioxidants' capacity to donate electrons to free radicals [55].

4.5. Minimum Inhibitory Concentration

The minimum inhibitory concentration (MIC) is a term used to describe the smallest quantity required to prevent microbial growth. The emergence of bacterial resistance and the expensive prices of sophisticated antimicrobial treatments have prompted scientists to look for medications that are effective, commercially feasible, and universally applicable. In our quest for a novel treatment option, we used the broth micro-dilution technique to assess the MIC of the *Vr*-Mn + Cu NPs against Gram-positive and negative bacteria. Six human pathogenic strains were examined utilizing *Vr*-Mn + Cu NPs at 1 mg/mL, using a serial dilution approach. Microbial growth inhibition was visible in 96-well plates after 24 h treatments, as shown in Table 1, and complete inhibition was found in the following order: *K. pneumonia*, 0.64 mg/mL; *S. aureus*, 0.64 mg/mL; *S. typhi*, 0.64 mg/mL; and *E. coli*, 0.32 mg/mL. The standard positive control (chloramphenicol) showed an MIC value of 0.1 mg/mL against *E. coli* and *K. pneumonia*, followed by 0.2 mg/mL against *S. typhi* and *S. aureus*. The aqueous extract was independently tested for MIC at the same dose of 0.1 mg/mL in this test; however, it did not prevent any microbial growth. The findings were consistent with prior research presented by the study referenced by [56]. Smaller nanoparticles often have a high surface area, which facilitates contact with the bacterial cell membrane and may ultimately change basic activities, such as penetrability and cell respiration, leading to cell death [57,58]. As a consequence, our findings indicated that the *Vr*-Mn + Cu NPs inhibited the development of all pathogens examined.

Table 1. MIC of *Vr*-Mn + Cu nanoparticles.

Minimum Inhibitory Concentration (MIC) (mg/mL)							
E. coli		*K. pneumonia*		*S. typhi*		*S. aureus*	
PC	NP	PC	NP	PC	NP	PC	NP
0.1	0.32	0.1	0.64	0.2	0.64	0.2	0.64

NP: nanoparticles; PC: positive control.

4.6. Antimicrobial Susceptibility Testing

The antibacterial activity of biogenic *Vr*-Mn + Cu NPs on four clinical pathogenic organisms (*E. coli*, *K. pneumonia*, *S. typhi* and *S. aureus*) was evaluated using the disk diffusion technique, and the findings were compared to the chemically generated results obtained by the *Vr*-Mn + Cu NPs. The disk diffusion technique demonstrates the amount of pathogenic microorganism susceptibility. For all microbes, the aqueous extract created a diffuse ring. The *Vr*-Mn + Cu NPs outperformed chemical NPs in terms of antibacterial activity, as shown in Figure 8. Table 2 shows the mean of three replicates of the diame-

ter of the inhibition zones (in millimeters) containing the *Vr*-Mn + Cu NPs' suspension. The *Vr*-Mn + Cu NPs had a greater inhibitory impact on *E. coli* (16.33 ± 0.57 mm). The inhibition zones for these kinds of *Vr*-Mn + Cu NPs were 14.0 ± 0.57 mm for *S. aureus*, 14.67 ± 1.57 mm for *K. pneumonia*, and 15.33 ± 0.57 mm for *S. typhi*. Chemically produced standards have lower inhibition zones. The AZ31 (Mg alloy) substrate with the Na-MMT coating against *E. coli* and *S. aureus* showed no inhibition zone, thereby confirming that AZ31 and Na-MMT had no antibacterial effects. The Zn-MMT coating against *E. coli* and *S. aureus* showed 22 mm and 32 mm inhibition zones, respectively [59]. Doped ZnO showed moderate to good activity against *E. coli* than bare ZnO [60]. In another study, bare ZnO displayed lesser antibacterial activity against the selected pathogens [61]. These findings support the greater antibacterial efficacy of the *Vr*-Mn + Cu NPs in comparison with the standard. Several modifications with a major effect on antibacterial qualities are often used in pharmaceutical, medical, and industrial wastewater treatment. Due to their small size, NPs have a larger surface area, which increases interaction with the bacterial cell membrane and changes key cell membrane functions, such as permeability and cell respiration, thereby resulting in cell death [14]. Earlier studies stated that the bacterial cells treated with bimetallic nanoparticles induced morphological changes and that the nanoparticles were found to disseminate on the bacterial cell surface [62]. In a recent study [63], green synthesized Cu NPs show 14 ± 0.15 inhibition zones for 100 μL; however, in current research, the bimetallic Mn + Cu nanoparticles show a greater inhibitory impact on *E. coli* (16.33 ± 0.57 mm). Moreover, the doped-Mn + Cu shows a high response with other clinically pathogenic organisms (*K. pneumonia*, *S. typhi* and *S. aureus*). In comparison with the Cu nanoparticles, the bimetallic particles are proven to be very efficient for antimicrobial applications.
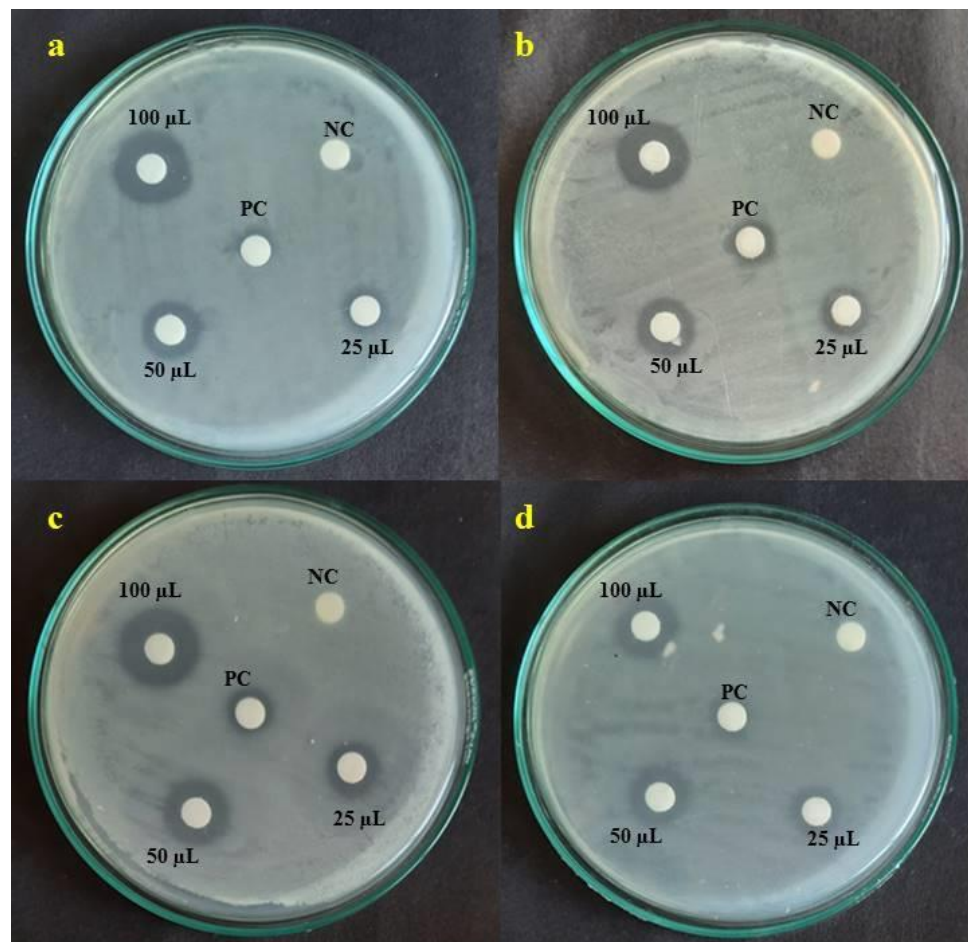

Figure 8. Antibacterial activity by *Vr*-Mn + Cu NPs with different strains: (**a**) *E. coli*; (**b**) *K. pneumonia*; (**c**) *S. typhi* and (**d**) *S. aureus*.

Table 2. Antibacterial activity of *Vr*-Mn + Cu nanoparticle compounds against pathogens.

Bacteria	Zone of Inhibition (mm)			
	Standard	25 μL	50 μL	100 μL
E. coli	7.33 ± 0.57	9.00 ± 1.00	11.33 ± 0.57	16.33 ± 0.57
K. pneumonia	8.67 ± 0.57	7.33 ± 0.57	10.67 ± 0.57	14.67 ± 1.57
S. typhi	10.7 ± 0.57	9.33 ± 0.57	11.33 ± 0.57	15.33 ± 0.57
S. aureus	9.00 ± 0.00	11.00 ± 1.00	12.66 ± 0.57	14.33 ± 0.57

4.7. Photocatalytic Dye Degradation Activity

Textile dye wastewater is a significant cause of water contamination. Among the wastewater pollutants emitted by the textile industry, methyl red is one of the dye effluents that may affect the environment. As a result, methyl red-contaminated water treatment is in great demand. Using *Vr*-Mn + Cu NPs as a catalyst, along with visible light irradiation, the photocatalytic degradation of methyl red, eriochrome black, and methyl orange was examined. It was revealed that $78.54 \pm 0.16\%$ (240 μg/mL) of methyl red, $87.67 \pm 0.06\%$ (240 μg/mL) of eriochrome black, and $69.79 \pm 0.36\%$ (240 μg/mL) of methyl orange decayed (Figure 9). Dye degradation is mostly induced by electrons and hole production on the catalyst surface during irradiation. As a consequence of a series of events, these electrons and holes combine to form OH radicals. OH radicals are highly reactive oxygen species that break down dye molecules into inorganic compounds. The deposition of NPs increases photocatalytic activity by minimizing electron and hole recombination during irradiation [64].
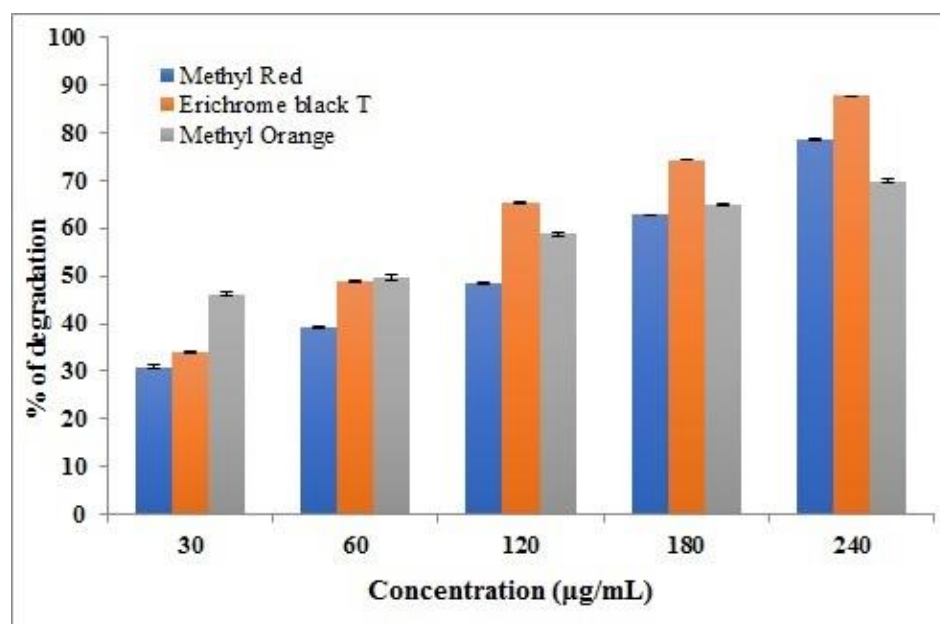
Figure 9. Plot of concentration vs. degradation percentage for dye degradation by *Vr*-Mn + Cu NPs.

4.8. Catalytic Efficiency

The catalytic efficiency of the *Vr*-Mn + Cu NPs were examined for the reduction of 4-nitrophenol as a pollutant. Figure 10a and b show the reduction percentage and ln (c_0/c_t) linear regression graph, with respect to the time of 4-nitrophenol reduction when using the *Vr*-Mn + Cu NPs. In this reduction process, 4-nitrophenol was reduced to 4-aminophenol, and this process was carried out at room temperature. During the process, 4-nitrophenol was changed to a phenolate ion as an intermediate, and finally, the intermediate was changed to 4-aminophenol (a lesser toxic chemical). The conversion

reaction was completed within 5 min, and the absorption was recorded for every 1 min interval during the reduction process. A sharp peak with high intensity around 400 nm was observed, which can be accredited to the 4-nitrophenol at 0 min and a broad peak was observed at 300 nm, which can be accredited to the 4-aminophenol at 3 min. When using 0.25 and 0.5 mg catalysts, they showed reduction percentages up to 94.90 and 96.27% at 4 min, respectively, and a 1 mg catalyst showed 97.58% efficiency at 2 min. It was found that, when the catalyst dosage increased, the concentration of 4-nitrophenol decreased rapidly. This is because, with more catalysts used, there will be more active surface sites available for a reaction with 4-nitrophenol. Figure 11 shows the absorbance graph with respect to the time of reduction of 4-nitrophenol when using the *Vr*-Mn + Cu NPs.
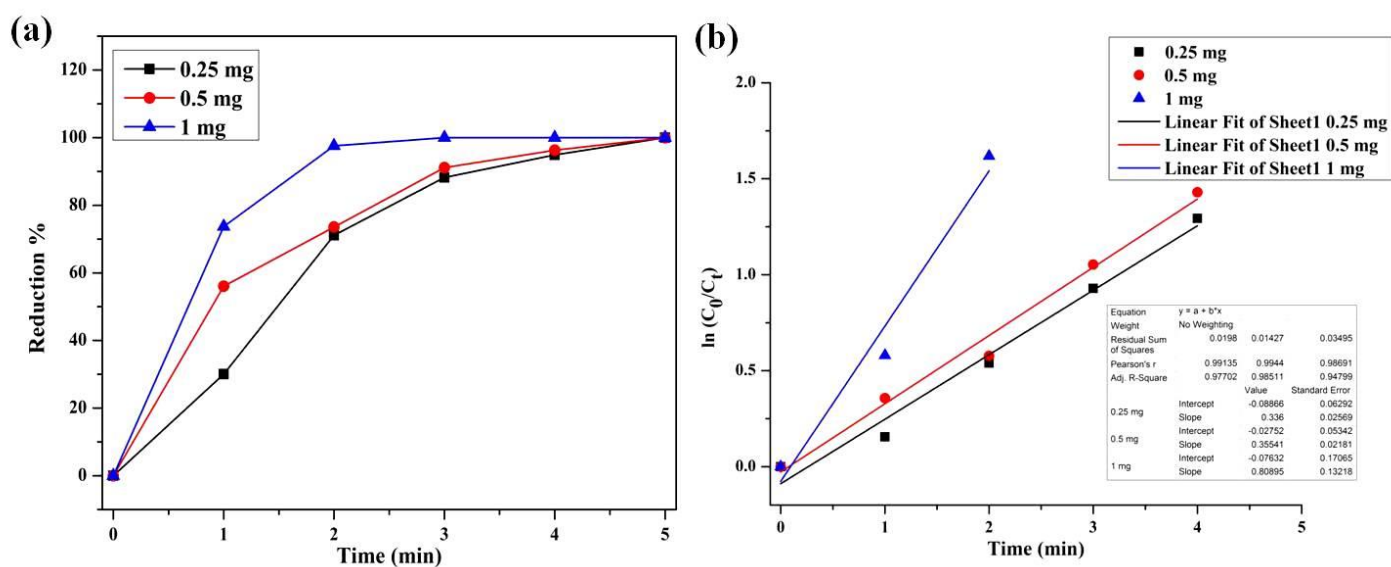

Figure 10. (**a**) Plot of time vs. percentage of 4-nitrophenol reduction by *Vr*-Mn + Cu NPs; (**b**) Plot of time vs. percentage ln (c_0/c_t) with linear regression.
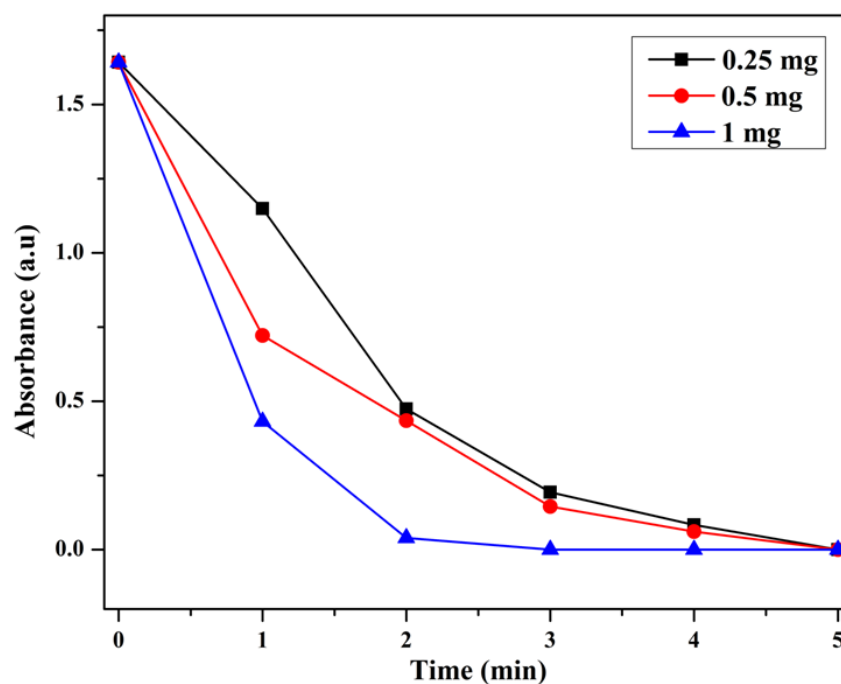

Figure 11. Plot of time vs. absorbance percentage for 4-nitrophenol reduction by *Vr*-Mn + Cu NPs.

5. Conclusions

The current work reveals a green and simple approach to manufacturing an Mn + Cu nanoparticle using *V. rosea* leaf extract, which acts as a reducing and stabilizing agent in the absence of organic solvents. We used a simple, natural, ecologically friendly, and non-hazardous substance in our synthetic method, eliminating the need for costly or hazardous chemical reagents and organic solvents. The FT–IR spectrum of the Mn + Cu NPs with *V. rosea* leaf extract revealed that alkaloids, flavonoids, and other compounds included in the extract were important in bioreduction. As an effective heterogeneous catalyst for the reduction of nitro compounds and organic dyes, the *Vr*-Mn + Cu NPs demonstrated outstanding antioxidant, antibacterial, photocatalytic, and catalytic activities.

Author Contributions: M.M.A., H.M.K., S.M. and M.W.A. did the experimental and characterization; M.W.-U.-R. and C.M.M. prepared the figures, data extraction revision. All the Authors contributed in writing the manuscript draft, editing and revision. All authors have read and agreed to the published version of the manuscript.

Institutional Review Board Statement: Not Applicable.

Informed Consent Statement: Not Applicable.

Data Availability Statement: Not Applicable.

Conflicts of Interest: The authors declare no conflict of interest.

References

1. Rayman, M.P. Selenium in cancer prevention: A review of the evidence and mechanism of action. *Proc. Nutr. Soc.* **2005**, *64*, 527–542. [CrossRef]
2. Watlington, K. *Emerging Nanotechnologies for Site Remediation and Wastewater Treatment*; Environmental Protection Agency: Washington, DC, USA, 2005.
3. Ferrari, M. Cancer nanotechnology: Opportunities and challenges. *Nat. Rev. Cancer* **2005**, *5*, 161–171. [CrossRef]
4. Khan, M.S.; Kim, H.; Kim, Y.; Ebina, Y.; Sugimoto, W.; Sasaki, T.; Osada, M. Scalable Design of Two-Dimensional Oxide Nanosheets for Construction of Ultrathin Multilayer Nanocapacitor. *Small* **2020**, *16*, 2003485. [CrossRef] [PubMed]
5. Khan, M.S.; Osada, M.; Kim, H.-J.; Ebina, Y.; Sugimoto, W.; Sasaki, T. High-temperature dielectric responses in all-nanosheet capacitors. *Jpn. J. Appl. Phys.* **2017**, *56*, 06GH09. [CrossRef]
6. Waqas Alam, M.; Khatoon, U.; Qurashi, A. Synthesis and characterization of Cu-SnO$_2$ nanoparticles deposited on glass using ultrasonic spray pyrolysis and their H2S sensing properties. *Curr. Nanosci.* **2012**, *8*, 919–924. [CrossRef]
7. Banach, M.; Pulit-Prociak, J. Proecological method for the preparation of metal nanoparticles. *J. Clean. Prod.* **2017**, *141*, 1030–1039. [CrossRef]
8. Devanesan, S.; AlSalhi, M.S.; Vishnubalaji, R.; Alfuraydi, A.A.; Alajez, N.M.; Alfayez, M.; Murugan, K.; Sayed, S.R.M.; Nicoletti, M.; Benelli, G. Rapid biological synthesis of silver nanoparticles using plant seed extracts and their cytotoxicity on colorectal cancer cell lines. *J. Clust. Sci.* **2017**, *28*, 595–605. [CrossRef]
9. Rajagopal, G.; Nivetha, A.; Sundar, M.; Panneerselvam, T.; Murugesan, S.; Parasuraman, P.; Kumar, S.; Ilango, S.; Kunjiappan, S. Mixed phytochemicals mediated synthesis of copper nanoparticles for anticancer and larvicidal applications. *Heliyon* **2021**, *7*, e07360. [CrossRef] [PubMed]
10. Burda, C.; Chen, X.; Narayanan, R.; El-Sayed, M.A. Chemistry and properties of nanocrystals of different shapes. *Chem. Rev.* **2005**, *105*, 1025–1102. [CrossRef]
11. Ferrando, R.; Jellinek, J.; Johnston, R.L. Nanoalloys: From theory to applications of alloy clusters and nanoparticles. *Chem. Rev.* **2008**, *108*, 845–910. [CrossRef]
12. Rodriguez, J.A.; Goodman, D.W. The nature of the metal-metal bond in bimetallic surfaces. *Science* **1992**, *257*, 897–903. [CrossRef]
13. Tao, F.; Grass, M.E.; Zhang, Y.; Butcher, D.R.; Renzas, J.R.; Liu, Z.; Chung, J.Y.; Mun, B.S.; Salmeron, M.; Somorjai, G.A. Reaction-driven restructuring of Rh-Pd and Pt-Pd core-shell nanoparticles. *Science* **2008**, *322*, 932–934. [CrossRef]
14. Rajagopal, G.; Manivannan, N.; Sundararajan, M.; Kumar, A.G.; Samuthirarajan, S.; Mathivanan, N.; Ilango, S. Biocompatibility assessment of silver chloride nanoparticles derived from Padina gymnospora and its therapeutic potential. *Nano Express* **2021**, *2*, 010010. [CrossRef]

15. Gupta, R.; Xie, H. Nanoparticles in daily life: Applications, toxicity and regulations. *J. Environ. Pathol. Toxicol. Oncol.* **2018**, *37*, 209–230. [CrossRef]

16. Hua, S.; de Matos, M.B.C.; Metselaar, J.M.; Storm, G. Current trends and challenges in the clinical translation of nanoparticulate nanomedicines: Pathways for translational development and commercialization. *Front. Pharmacol.* **2018**, *9*, 790. [CrossRef] [PubMed]

17. Elechiguerra, J.L.; Burt, J.L.; Morones, J.R.; Camacho-Bragado, A.; Gao, X.; Lara, H.H.; Yacaman, M.J. Interaction of silver nanoparticles with HIV-1. *J. Nanobiotechnol.* **2005**, *3*, 6. [CrossRef]

18. Khan, M.; Al-Marri, A.H.; Khan, M.; Shaik, M.R.; Mohri, N.; Adil, S.F.; Kuniyil, M.; Alkhathlan, H.Z.; Al-Warthan, A.; Tremel, W. Green approach for the effective reduction of graphene oxide using *Salvadora persica* L. root (Miswak) extract. *Nanoscale Res. Lett.* **2015**, *10*, 281. [CrossRef] [PubMed]

19. He, Y. Synthesis of ZnO nanoparticles with narrow size distribution under pulsed microwave heating. *China Particuology* **2004**, *2*, 168–170. [CrossRef]

20. Chun, H.; Yizhong, W. Decolorization and biodegradability of photocatalytic treated azo dyes and wool textile wastewater. *Chemosphere* **1999**, *39*, 2107–2115. [CrossRef]

21. Kiwi, J.; Pulgarin, C.; Peringer, P.; Grätzel, M. Beneficial effects of homogeneous photo-Fenton pretreatment upon the biodegradation of anthraquinone sulfonate in waste water treatment. *Appl. Catal. B Environ.* **1993**, *3*, 85–99. [CrossRef]

22. Li, J.; Xu, Y.; Liu, Y.; Wu, D.; Sun, Y. Synthesis of hydrophilic ZnS nanocrystals and their application in photocatalytic degradation of dye pollutants. *China Particuol.* **2004**, *2*, 266–269. [CrossRef]

23. Hoffmann, M.R.; Martin, S.T.; Choi, W.; Bahnemann, D.W. Environmental applications of semiconductor photocatalysis. *Chem. Rev.* **1995**, *95*, 69–96. [CrossRef]

24. Basharat, M.; Khan, M.S.; Abbas, Y.; Zhang, S.; Ma, H.; Wu, Z.; Liu, W. Cyclotriphosphazene (P_3N_3) hybrid framework for aggregation induced photocatalytic hydrogen evolution and degradation of rhodamine B. *Mater. Chem. Front.* **2020**, *4*, 3216–3225. [CrossRef]

25. Irfan, M.F.; Qurashi, A.; Alam, M.W. Metal oxide nanostructures and nanocomposites for selective catalytic reduction of NOx: A review. *Arab. J. Sci. Eng.* **2010**, *35*, 79–92.

26. Aarthi, T.; Narahari, P.; Madras, G. Photocatalytic degradation of Azure and Sudan dyes using nano TiO_2. *J. Hazard. Mater.* **2007**, *149*, 725–734. [CrossRef] [PubMed]

27. Matthews, R.W. Kinetics of photocatalytic oxidation of organic solutes over titanium dioxide. *J. Catal.* **1988**, *111*, 264–272. [CrossRef]

28. Dahl, J.A.; Maddux, B.L.S.; Hutchison, J.E. Toward greener nanosynthesis. *Chem. Rev.* **2007**, *107*, 2228–2269. [CrossRef]

29. Valsalam, S.; Agastian, P.; Esmail, G.A.; Ghilan, A.-K.M.; Al-Dhabi, N.A.; Arasu, M.V. Biosynthesis of silver and gold nanoparticles using Musa acuminata colla flower and its pharmaceutical activity against bacteria and anticancer efficacy. *J. Photochem. Photobiol. B Biol.* **2019**, *201*, 111670. [CrossRef]

30. Sowndarya, P.; Ramkumar, G.; Shivakumar, M.S. Green synthesis of selenium nanoparticles conjugated Clausena dentata plant leaf extract and their insecticidal potential against mosquito vectors. *Artif. Cells Nanomed. Biotechnol.* **2017**, *45*, 1490–1495. [CrossRef]

31. Jaleel, C.A.; Gopi, R.; Lakshmanan, G.M.A.; Panneerselvam, R. Triadimefon induced changes in the antioxidant metabolism and ajmalicine production in *Catharanthus roseus* (L.) G. Don. *Plant Sci.* **2006**, *171*, 271–276. [CrossRef]

32. Jordan, M.A.; Thrower, D.; Wilson, L. Mechanism of inhibition of cell proliferation by Vinca alkaloids. *Cancer Res.* **1991**, *51*, 2212–2222.

33. Kulkarni, R.N.; Baskaran, K.; Chandrashekara, R.S.; Kumar, S. Inheritance of morphological traits of periwinkle mutants with modified contents and yields of leaf and root alkaloids. *Plant Breed.* **1999**, *118*, 71–74. [CrossRef]

34. Ahmed, M.F.; Kazim, S.M.; Ghori, S.S.; Mehjabeen, S.S.; Ahmed, S.R.; Ali, S.M.; Ibrahim, M. Antidiabetic activity of Vinca rosea extracts in alloxan-induced diabetic rats. *Int. J. Endocrinol.* **2010**, *2010*, 841090. [CrossRef]

35. Gülçin, İ. Antioxidant activity of eugenol: A structure–activity relationship study. *J. Med. Food* **2011**, *14*, 975–985. [CrossRef]

36. Cetinkaya, Y.; Göçer, H.; Menzek, A.; Gülçin, İ. Synthesis and antioxidant properties of (3, 4-dihydroxyphenyl)(2,3,4-trihydroxyphenyl) methanone and its derivatives. *Arch. Pharm.* **2012**, *345*, 323–334. [CrossRef]

37. Halliwell, B.; Gutteridge, J.M.C. Formation of a thiobarbituric-acid-reactive substance from deoxyribose in the presence of iron salts: The role of superoxide and hydroxyl radicals. *FEBS Lett.* **1981**, *128*, 347–352. [CrossRef]

38. Benzie, I.F.F.; Strain, J.J. The ferric reducing ability of plasma (FRAP) as a measure of "antioxidant power": The FRAP assay. *Anal. Biochem.* **1996**, *239*, 70–76. [CrossRef]

39. Zhu, Q.Y.; Holt, R.R.; Lazarus, S.A.; Orozco, T.J. Inhibitory effects of cocoa flavanols and procyanidin oligomers on free radical-induced erythrocyte hemolysis. *Exp. Biol. Med.* **2002**, *227*, 321–329. [CrossRef] [PubMed]

40. Garibo, D.; Borbón-Nuñez, H.A.; de León, J.N.D.; Mendoza, E.G.; Estrada, I.; Toledano-Magaña, Y.; Tiznado, H.; Ovalle-Marroquin, M.; Soto-Ramos, A.G.; Blanco, A. Green synthesis of silver nanoparticles using Lysiloma acapulcensis exhibit high-antimicrobial activity. *Sci. Rep.* **2020**, *10*, 12805. [CrossRef] [PubMed]

41. Jayaraj, A.J.; Uchimahali, J.; Gnanasundaram, T.; Thirumal, S. Evaluation of antimicrobial activity and phytochemicals analysis of whole plant extract of Vinca rosea. *Evaluation* **2019**, *12*, 132–136.

42. Rafique, M.; Shaikh, A.J.; Rasheed, R.; Tahir, M.B.; Gillani, S.S.A.; Usman, A.; Imran, M.; Zakir, A.; Khan, Z.U.H.; Rabbani, F. Aquatic biodegradation of methylene blue by copper oxide nanoparticles synthesized from Azadirachta indica leaves extract. *J. Inorg. Organomet. Polym. Mater.* **2018**, *28*, 2455–2462. [CrossRef]

43. Dehvari, K.; Li, J.-D.; Chang, J.-Y. Bovine serum albumin-templated synthesis of manganese-doped copper selenide nanoparticles for boosting targeted delivery and synergistic photothermal and photodynamic therapy. *ACS Appl. Bio Mater.* **2019**, *2*, 3019–3029. [CrossRef]

44. Hemalatha, C.; Babu, K.S.; Rao, G.N. Mn Doped CuO Nanoparticles Synthesized by Spray Pyrolysis: Structural, Optical and Magnetic Characterization. *J. Magn.* **2020**, *25*, 330–334. [CrossRef]

45. Nasrollahzadeh, M.; Sajjadi, M.; Sajadi, S.M. Biosynthesis of copper nanoparticles supported on manganese dioxide nanoparticles using Centella asiatica L. leaf extract for the efficient catalytic reduction of organic dyes and nitroarenes. *Chin. J. Catal.* **2018**, *39*, 109–117. [CrossRef]

46. Alsaheb, M.A.; Alsahib, S.A. Synthesis, Characterization and polymerization of 1Hpyrazolo [1,2-b] phthalazine-5, 10-dione derivatives Using CuO nanoparticle Oxide from Natural Source as Catalyst. *Drug Deliv.* **2020**, *10*, 530–536.

47. Clogston, J.D.; Patri, A.K. Zeta potential measurement. In *Characterization of Nanoparticles Intended for Drug Delivery*; Springer: Cham, Switzerland, 2011; pp. 63–70.

48. Agarwal, P.; Gupta, R.; Agarwal, N. Advances in synthesis and applications of microalgal nanoparticles for wastewater treatment. *J. Nanotechnol.* **2019**, *2019*, 7392713. [CrossRef]

49. Devatha, C.P.; Jagadeesh, K.; Patil, M. Effect of Green synthesized iron nanoparticles by Azardirachta Indica in different proportions on antibacterial activity. *Environ. Nanotechnol. Monit. Manag.* **2018**, *9*, 85–94. [CrossRef]

50. Sundar, M.; Suresh, S.; Lingakumar, K. Influence of Caralluma adscendens Var. attenuata cold cream on UV-B damaged skin epidermal cells: A novel approach. *3 Biotech* **2021**, *11*, 155. [CrossRef]

51. Satheeshkumar, M.K.; Kumar, E.R.; Indhumathi, P.; Srinivas, C.; Deepty, M.; Sathiyaraj, S.; Suriyanarayanan, N.; Sastry, D.L. Structural, morphological and magnetic properties of algae/CoFe$_2$O$_4$ and algae/Ag-Fe-O nanocomposites and their biomedical applications. *Inorg. Chem. Commun.* **2020**, *111*, 107578. [CrossRef]

52. Korycka-Dahl, M.; Richardson, T. Photogeneration of superoxide anion in serum of bovine milk and in model systems containing riboflavin and amino acids. *J. Dairy Sci.* **1978**, *61*, 400–407. [CrossRef]

53. Yang, H.; Yang, R.; Zhang, P.; Qin, Y.; Chen, T.; Ye, F. A bimetallic (Co/2Fe) metal-organic framework with oxidase and peroxidase mimicking activity for colorimetric detection of hydrogen peroxide. *Microchim. Acta* **2017**, *184*, 4629–4635. [CrossRef]

54. Zhou, Y.; Zhang, Y.; Hu, X. Novel zero-valent Co–Fe encapsulated in nitrogen-doped porous carbon nanocomposites derived from CoFe$_2$O$_4$@ ZIF-67 for boosting 4-chlorophenol removal via coupling peroxymonosulfate. *J. Colloid Interface Sci.* **2020**, *575*, 206–219. [CrossRef]

55. Shimada, K.; Fujikawa, K.; Yahara, K.; Nakamura, T. Antioxidative properties of xanthan on the autoxidation of soybean oil in cyclodextrin emulsion. *J. Agric. Food Chem.* **1992**, *40*, 945–948. [CrossRef]

56. Abalkhil, T.A.; Alharbi, S.A.; Salmen, S.H.; Wainwright, M. Bactericidal activity of biosynthesized silver nanoparticles against human pathogenic bacteria. *Biotechnol. Biotechnol. Equip.* **2017**, *31*, 411–417. [CrossRef]

57. Song, H.Y.; Ko, K.K.; Oh, L.H.; Lee, B.T. Fabrication of silver nanoparticles and their antimicrobial mechanisms. *Eur. Cells Mater.* **2006**, *11*, 58.

58. Panáček, A.; Kvitek, L.; Prucek, R.; Kolář, M.; Večeřová, R.; Pizúrová, N.; Sharma, V.K.; Nevěčná, T.J.; Zbořil, R. Silver colloid nanoparticles: Synthesis, characterization, and their antibacterial activity. *J. Phys. Chem. B* **2006**, *110*, 16248–16253. [CrossRef]

59. Zou, Y.-H.; Wang, J.; Cui, L.-Y.; Zeng, R.-C.; Wang, Q.-Z.; Han, Q.-X.; Qiu, J.; Chen, X.-B.; Chen, D.-C.; Guan, S.-K.; et al. Corrosion resistance and antibacterial activity of zinc-loaded montmorillonite coatings on biodegradable magnesium alloy AZ31. *Acta Biomater.* **2019**, *98*, 196–214. [CrossRef]

60. Senthilraja, A.; Krishnakumar, B.; Hariharan, R.; Sobral, A.J.F.; Surya, C.; Agnel Arul John, N.; Shanthi, M. Synthesis and characterization of bimetallic nanocomposite and its photocatalytic, antifungal and antibacterial activity. *Sep. Purif. Technol.* **2018**, *202*, 373–384. [CrossRef]

61. Dhillon, G.S.; Kaur, S.; Brar, S.K. Facile fabrication and characterization of chitosan-based zinc oxide nanoparticles and evaluation of their antimicrobial and antibiofilm activity. *Int. Nano Lett.* **2014**, *4*, 107. [CrossRef]

62. Zhao, X.; Jia, Y.; Dong, R.; Deng, J.; Tang, H.; Hu, F.; Liu, S.; Jiang, X. Bimetallic nanoparticles against multi-drug resistant bacteria. *Chem. Commun.* **2020**, *56*, 10918–10921. [CrossRef]

63. Jayarambabu, N.; Akshaykranth, A.; Rao, T.V.; Rao, K.V.; Kumar, R.R. Green synthesis of Cu nanoparticles using Curcuma longa extract and their application in antimicrobial activity. *Mater. Lett.* **2020**, *259*, 126813. [CrossRef]

64. Patra, S.; Roy, E.; Madhuri, R.; Sharma, P.K. Agar based bimetallic nanoparticles as high-performance renewable adsorbent for removal and degradation of cationic organic dyes. *J. Ind. Eng. Chem.* **2016**, *33*, 226–238. [CrossRef]